The Gemini Planet Imager

Bruce Macintosh, et al.

May 15, 2006

Disclaimer

The Gemini Planet Imager

Bruce Macintosh [*ab], James Graham [ac], David Palmer [ab], Rene Doyon [d], Don Gavel [ae], James Larkin [af], Ben Oppenheimer [ag], Leslie Saddlemyer [h], J. Kent Wallace [ai], Brian Bauman [ab], Julia Evans [ab], Darren Erikson [h], Katie Morzinski [ae], Donald Phillion [b], Lisa Poyneer [ab] Anand Sivaramakrishnan [ag], Remi Soummer [ag], Simon Thibault [j], Jean-Pierre-Veran [h]

[a] NSF Center for Adaptive Optics
[b] Lawrence Livermore National Laboratory, 7000 East Ave., Livermore, CA 94551
[c] Department of Astronomy, University of California at Berkeley, Berkeley, CA 94720
[d] Universite de Montreal, Department de Physique, Montreal, QC, H3C 3J7, Canada
[e] UC Santa Cruz, 1156 High Street, Santa Cruz, CA
[f] Department of Physics and Astronomy, UC Los Angeles, Los Angeles, CA 90095
[g] Department of Astrophysics, American Museum of Natural History, New York, NY 10024
[h] Herzberg Institute of Astrophysics, 5071 West Saanich Road, Victoria, BC V8X 4M6
[i] Jet Propulsion Laboratory, California Institute of Technology, Pasadena, CA 91109
[j] Immervision, 2020 University, Suite 2420, Montreal, QC H3A 2A5, Canada

ABSTRACT

The next major frontier in the study of extrasolar planets is direct imaging detection of the planets themselves. With high-order adaptive optics, careful system design, and advanced coronagraphy, it is possible for an AO system on a 8-m class telescope to achieve contrast levels of 10^{-7} to 10^{-8}, sufficient to detect warm self-luminous Jovian planets in the solar neighborhood. Such direct detection is sensitive to planets inaccessible to current radial-velocity surveys and allows spectral characterization of the planets, shedding light on planet formation and the structure of other solar systems. We have begun the construction of such a system for the Gemini Observatory. Dubbed the Gemini Planet Imager (GPI), this instrument should be deployed in 2010 on the Gemini South telescope. It combines a 2000-actuator MEMS-based AO system, an apodized-pupil Lyot coronagraph, a precision infrared interferometer for real-time wavefront calibration at the nanometer level, and a infrared integral field spectrograph for detection and characterization of the target planets. GPI will be able to achieve Strehl ratios > 0.9 at 1.65 microns and to observe a broad sample of science targets with I band magnitudes less than 8. In addition to planet detection, GPI will also be capable of polarimetric imaging of circumstellar dust disks, studies of evolved stars, and high-Strehl imaging spectroscopy of bright targets. We present here an overview of the GPI instrument design, an error budget highlighting key technological challenges, and models of the system performance.

Keywords: Adaptive optics, extrasolar planets, coronagraph

1. INTRODUCTION AND SYSTEM OVERVIEW

More than 140 extrasolar planets have been detected through Doppler techniques[1] and have begun a revolution in our understanding of planetary systems. However, this revolution is still incomplete: several competing theories of planet formation and migration exist based on the observations of planets in unexpected regions. The ability to directly detect extrasolar planets would be a powerful complement to Doppler techniques if it allowed us to probe planets in orbits (5-50 AU) with periods too long for Doppler searches. Spectral characterization of directly-detected extrasolar planets would allow measurements of their radius, temperature, and surface gravity. Current AO systems are limited to contrasts of 10^{-5}-10^{-6} at large (>1 arcsecond) angles. This can allow detection of young (<10 Myr) planets[2] in exotic circumstances, but since young stars are distant these will necessarily only be visible in wide (>50 AU) orbits and hence

---

[*] bmac@igpp.llnl.gov

involve atypical formation scenarios. Contrasts of 10^{-7}-10^{-8}, though insufficient to detect a mature Jupiter-analog, can detect more massive planets through their self-luminosity to ages of 1 Gyr or more.

Achieving such a contrast will require a new type of astronomical system, dedicated specifically to high-contrast imaging rather than being optimized for general use. The Gemini Planet Imager (GPI) is such an instrument. GPI has four major components. The primary AO system sharply attenuates atmospheric wavefront errors, optimized not for maximum Strehl but for best performance in the "dark hole" region and minimal systematic errors. Diffraction is suppressed through an apodized-pupil Lyot coronagraph (APLC) which combines a conventional Lyot-type design with mild pupil apodization to shape the intensity in the Lyot plane. Tightly integrated with the coronagraph is a infrared interferometric wavefront sensor. This serves as a calibration system, measuring the time-averaged wavefront during a science exposure. This information can be used to modify the main AO system control point to remove residual static errors and to reconstruct the final point spread function (PSF.) Finally, the science light is fed into a near-IR Integral Field Unit (IFU) imaging spectrograph that serves as the only science instrument.

Table 1 lists the key properties of the GPI system and Figure 1 shows a schematic overview. Light enters at the top right and is relayed between the two deformable mirrors (2.2). The output of this AO relay is a converging f/64 beam with a pupil at a finite distance. Visible light (<0.95 microns) is split off to the spatially-filtered Shack-Hartmann wavefront sensor (2.1). The IR light passes through a pupil plane at which we place input pupil masks such as apodizers. It then continues to converge to the f/64 focus. At this plane we place reflective occulting masks; the core of the PSF passes through a hole in the occulting mask and into the calibration system while the outer part of the PSF is reflected. The resulting beam is collimated and split between the calibration system and the science integral field unit. The beam enters the IFU collimated, with the (selectable) cryogenic Lyot stop pupil located just inside the dewar.

Table 1: Key system parameters

| AO subsystem	
Primary deformable mirror	4096-actuator Boston Micromachines MEMS
Subaperture size	d =18 cm (N = 44 subapertures across primary mirror)
Wave front sensor type	Spatially-filtered Shack-Hartmann Wave Front Sensor (SFWFS)
Wave front sensor CCD	128 x 128 pixels (goal: 180x180)
Maximum frame rate	2500 Hz
Reconstructor	Optimal Fourier Transform Reconstructor
Limting magnitude	I < 8 mag. (goal: I < 9 mag.)
Optics	
Surface quality	<5 nm RMS WFE per optic
Coronagraph subsystem	
Type	Apodized-Pupil Lyot Coronagraph (APLC)
Inner working distance	~3 λ/D
Transmission	> 60%
Calibration subsystem	
Type	Infrared interferometeric wave front sensor
Wavelength range	1-2.4 µm
Wave front measurement precision	1 nm RMS in controlled frequency range
Science Instrument	
Type	Lenslet-based integral field spectrograph
Lenslet size	0.014 x 0.014 arcseconds
Field of view	3.6 x 3.6 arcseconds
Spectral resolution	$\Delta\lambda/\lambda \sim 40$
Spectral coverage	One of Y, J, H or K band per exposure (20% bandwidth)
Detector	HAWAII-II RG
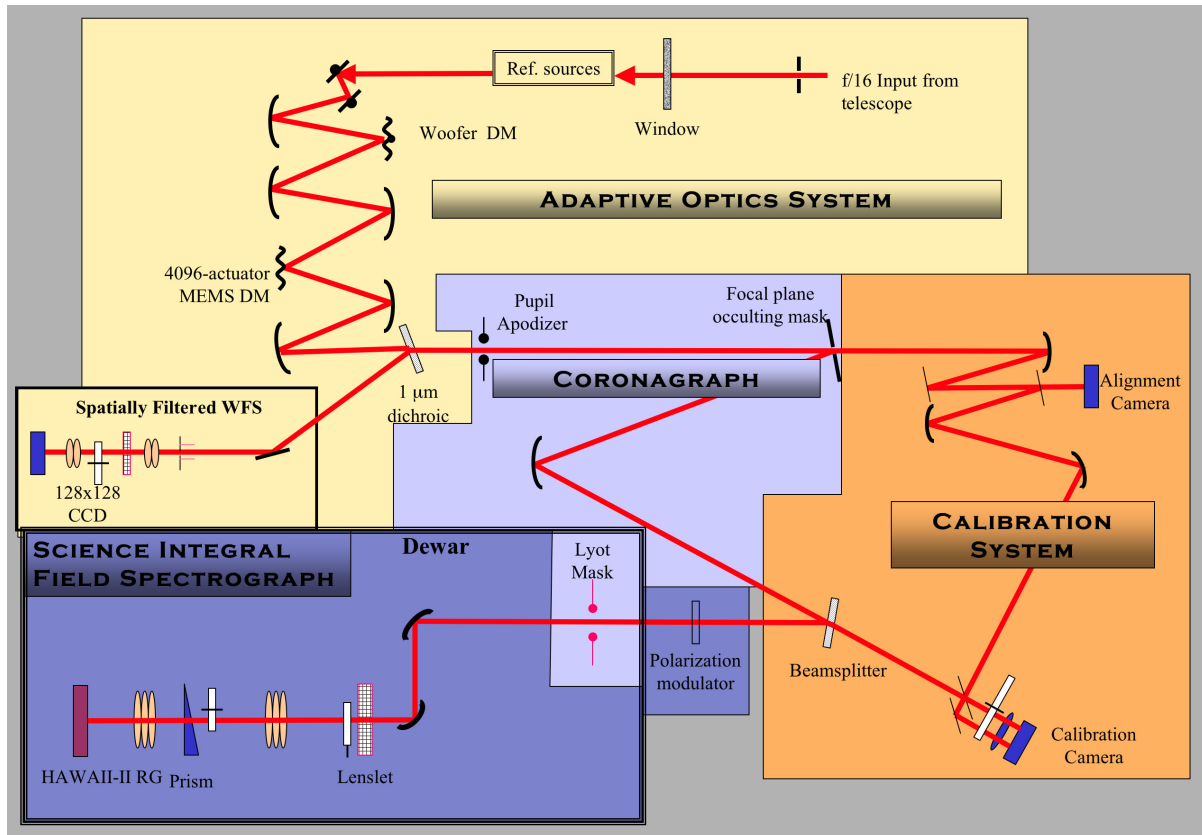
Figure 1: Schematic layout of the Gemini Planet Imager
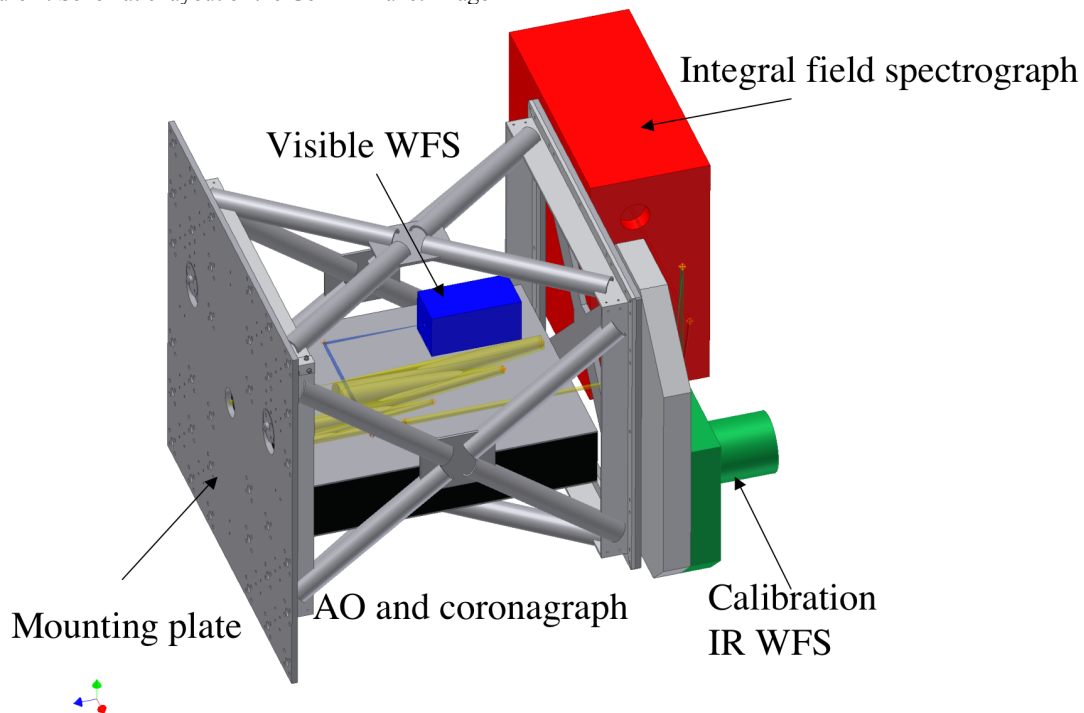
Figure 2: CAD image of GPI. The Gemini Instrument Support Structure mounting plate (left) is 1.3 meters on a side.

2. AO SYSTEM

2.1 Wavefront sensor

The primary wavefront sensor is a visible-light spatially-filtered Shack-Hartmann wavefront sensor (SFWFS)[3]. The square spatial filter is matched to the subaperture sampling λ/d and prevents aliasing of dynamic and static wavefront errors. By operating at the long end of the silicon CCD response (0.7-0.9 microns), spatial filter performance is maximized and chromatic errors are reduced at some cost to limiting magnitude on blue targets. In the baseline design, each lenslet is matched to a 2x2 quad cell. Although quad cells are inherently nonlinear, the optical design and component choices minimize non-common path errors (<10 nm RMS). Combined with the stable response of a SFWFS with d~r0 (spot size is independent of r0), this reduces PSF changes due to spot size variations. Since AO servo lag is a major source of scattered light within the dark hole, it is important for the system to operate as fast as possible; the current CCD selection is a Lincoln Labs CCID18 1282 CCD. The pnCCD[4] is also attractive for its excellent red QE and small charge diffusion. Zero-noise CCDs such as the E2V L3 device are interesting, but the enhanced performance on very dim targets would be offset by likely lower frame rates and concerns about gain stability.

2.2 Reconstructor

The wavefront controller for GPI uses an adaptive algorithm called Optimal Fourier Control (OFC).[5] At each time step, the slope measurements obtained from the spatially filtered Shack-Hartmann WFS are reconstructed into a residual phase estimate using the computationally efficient Fourier Transform Reconstruction (FTR) method. This method reconstructs the phase in Fourier modes – a convenient modal set for ExAO, since each Fourier mode scatters light to a specific spatial location in the PSF. Telemetry of the closed-loop modal coefficients is saved, and then used in a supervisory process to estimate the temporal PSDs of the atmosphere and the noise. The optimal control loop gain which minimizes the residual error power is estimated at ~ 1 Hz. This gain is used in the reconstruction to provide wavefront control which minimizes the PSF intensity by location in the controllable region.
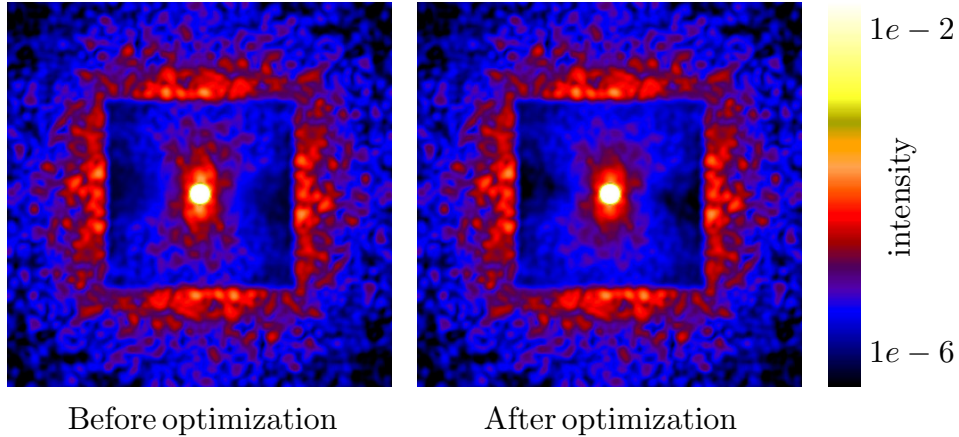

Before optimization   After optimization

Figure 3: Simulated 1-second PSFs before and after gain optimization for an *I*=6 mag. star at a frame rate of 2 kHz. Optimizing the gains reduces average SPF intensity in the dark hole by 40%.

Fig. 1 shows two 1-second PSFs obtained from the GPI end-to-end AO simulator code for the case of 2 kHz operation and a guide star *I*=6 mag. The first PSF is with a uniform gain of 0.3 on all modes, the second is on the same atmosphere but with the optimized gains as determined in simulation. The new gains range from 0.15 to 0.52. Gain optimization reduces PSF intensity in nearly all regions inside the dark hole. Wavefront errors from temporal lags produce the 'butterfly' region along the y-axis, along the direction of the dominant wind layer. Increased gains here lead to dimmer speckles after optimization. Wavefront errors from WFS measurement noise are present everywhere and fill in the dark regions along the x-axis; reducing the gains in this region results in a dimmer and smoother PSF.

2.3 Real-time computer

Using the efficient Fourier Transform Reconstructor, our computational requirements peak at 3 billion operations per second for a 2500 Hz system, with I/O peaking at 150 million read/writes per second. This is within the reach of current

off-the-shelf general purpose computers, e.g. a quad Intel Xeon-based server. Our baseline architecture is shown in Figure 4. Wavefront sensor frames enter through the PIC-X bus. DM commands are sent out through a PCI/VME bus bridge to four custom multichannel high-voltage DAC boards that connect directly to the MEMS mirror.

2.4 Deformable mirrors

Commands from the wavefront sensor drive a MEMS deformable mirror (DM) with N=44 actuators across the primary mirror. Development of this DM is currently underway, based on the N=32 Boston Micromachines mirror[6]. Actuator yield was a significant concern in the early Boston DMs, but recent laboratory testing has shown yields of ~99.5% with no dead actuators in the central 90% inscribed circle of the mirror. The DM will be manufactured in a 64x64 format to increase the probability of finding a useable circular region. The MEMS DM will have only 3-4 microns (surface) stroke, insufficient to fully correct the atmosphere on a 8-m telescope. We will therefore operate a woofer/tweeter architecture, offloading low-frequency modes from the MEMS to bimorph DM which will also provide tip/tilt correction.
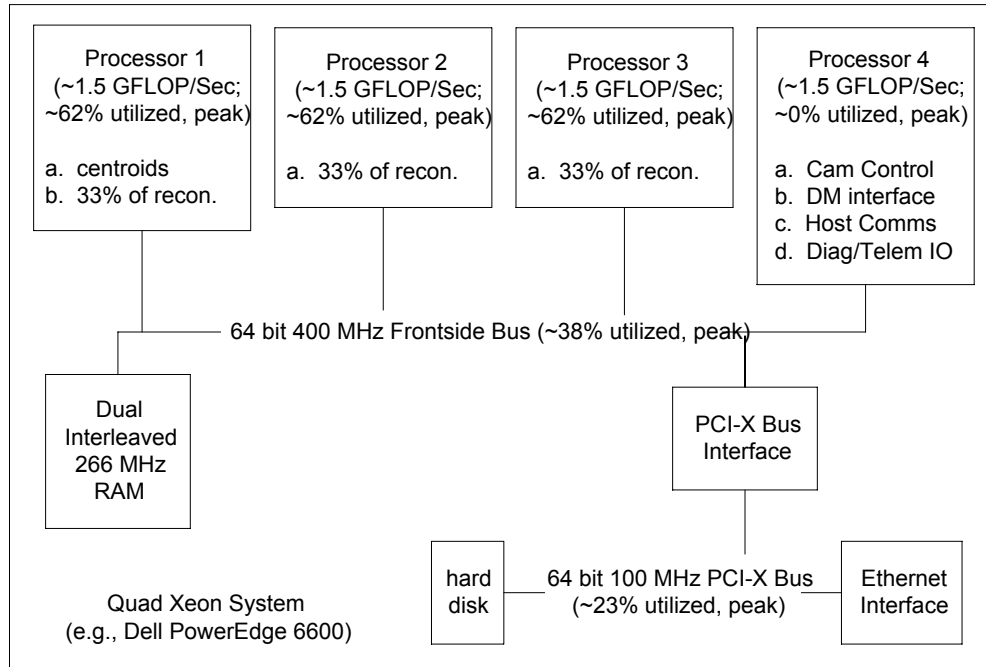

Figure 4:GPI realtime computer architecture

3. CORONAGRAPH

Light is scattered into the halo of the point spread function both by wavefront errors and by diffraction[7] – even a perfect telescope in space will have a bright Airy pattern that will prevent detection of planets. Controlling this diffraction is the role of a coronagraph. Driven in part by the Terrestrial Planet Finder requirements, a wide variety of new coronagraph architectures have been designed in recent years. Many of these are impractical with a ground-based telescope with a central obscuration, however. Classic Lyot coronagraphs do not perform well enough to take advantage of GPI's high-quality wavefronts. Band-limited Lyot coronagraphs[8] (BLC), though capable of near-perfect diffraction cancellation, require high-ND occultors that are difficult to manufacture for use at near-IR wavelengths; binary BLC versions are unproven in the near-IR and may suffer from wave-optics effects. Pure greyscale apodizers are similarly hard to manufacture. Shaped-pupil coronagraphs are a manufacturable alternative to apodizers but only suppress diffraction over a limited area; in addition to restricting science coverage, in the AO case (where out-of-band wavefront errors may be large), high-order crosstalk effects in the PSF cause light to bleed into the dark region from the convolution of the wavefront-control dark hole with the diffraction-suppressed region. We have selected as a baseline the Apodized Pupil Lyot Coronagraph (APLC)[9].

The classic Lyot Coronagraph (LC) involves a focal plane stop or mask (FPM) that blocks most of the light of the central star (or the Sun, as in the case for the original instrument), followed by a reimaged pupil plane. Diffraction by the focal plane stop serves to place the remaining light from the blocked star into a ring around the edge of the pupil. The eponymous Lyot stop is inserted into this pupil plane to downsize the pupil and block this diffracted starlight. Recently, researchers in high contrast imaging have noted that if the pupil plane preceding the Lyot coronagraph's FPM were to be apodized, the suppression of the PSF in the final focal plane could be greatly improved.

To understand the APLC and why apodization improves performance, consider what a coronagraph does to the wave front amplitude of an on-axis point source in the final Lyot stop plane. A mathematical formalism can be derived that treats the field amplitude in this final pupil plane as the difference between the first pupil's amplitude distribution and the distribution caused by diffraction due to the FPM. Thus, to optimize the performance of a Lyot-style coronagraph, these two amplitude distributions must be as closely matched as possible. By gently apodizing the entrance pupil in a manner matched to the occulter diameter this difference can be minimized over the aperture better than in the classic Lyot case[9]. Figure 5 shows the transmission profile for a typical mask. The maximum attenuation required is ~90%, much lower than for a BLC or classic apodizer. This level of apodization is attainable using High Energy Beam Sensitive (HEBS) glass and possibly with metal deposited on glass. Each waveband (*YJHK*) will require its own customized apodizer.
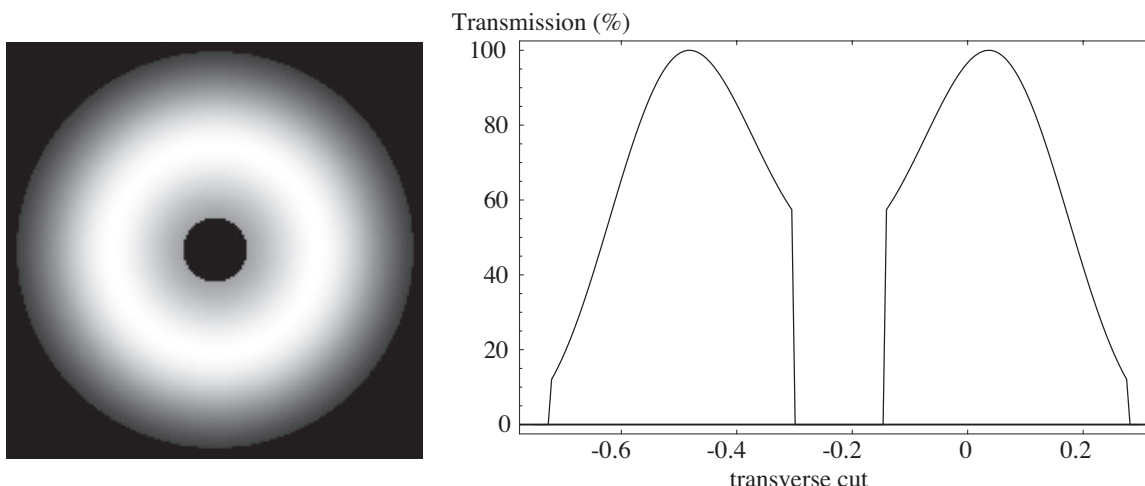

Figure 5: Example of apodizer transmission for the Gemini Telescope geometry[9]. The minimum intensity transmission is 12% at the edges, and throughput is high: 63%. A classical Lyot coronagraph with an undersized Lyot stop has a typical throughput of 40% in contrast. The matched FPM has a diameter of 4.7 λ/D.

PSF suppression by an APLC is wavelength-dependent, so careful optimization over the filter bandpass must be carried out. Figure 6 shows broad-band PSFs for the APLC without spectral optimization.

All three coronagraph planes – input apodizer, focal plane mask, and Lyot stop – are located inside selectable wheels. The two pupil planes also can be rotated to match the orientation of the telescope (e.g. secondary supports.)

4. INFRARED CALIBRATION WFS

Small wavefront errors due to chromatic effects, changes in non-common-path optics, initial calibration errors, etc., produce quasi-static speckles that can completely swamp the signal from a planet. To achieve 10^{-7} contrast with GPI we require these errors to be ~1 nm over the controlled range of spatial frequencies – an extremely challenging goal. To achieve this, we will integrate a second high-precision IR wavefront sensor designed to measure the wavefront after the coronagraph focal plane.

The selected architecture is a modified Mach-Zehnder interferometer. Figure 7 shows a simple version of the calibration sensor. Light from the core of the PSF is removed at the coronagraph focal plane to provide a reference wavefront. Off-axis (science) light is sampled by a neutral beamsplitter and interfered with the reference light to provide wavefront measurements.[10]

r(arcsec)

0   0.5   1.   1.5

log(I)

- PSF
- Lyot
- APLC
- APLC no WFE

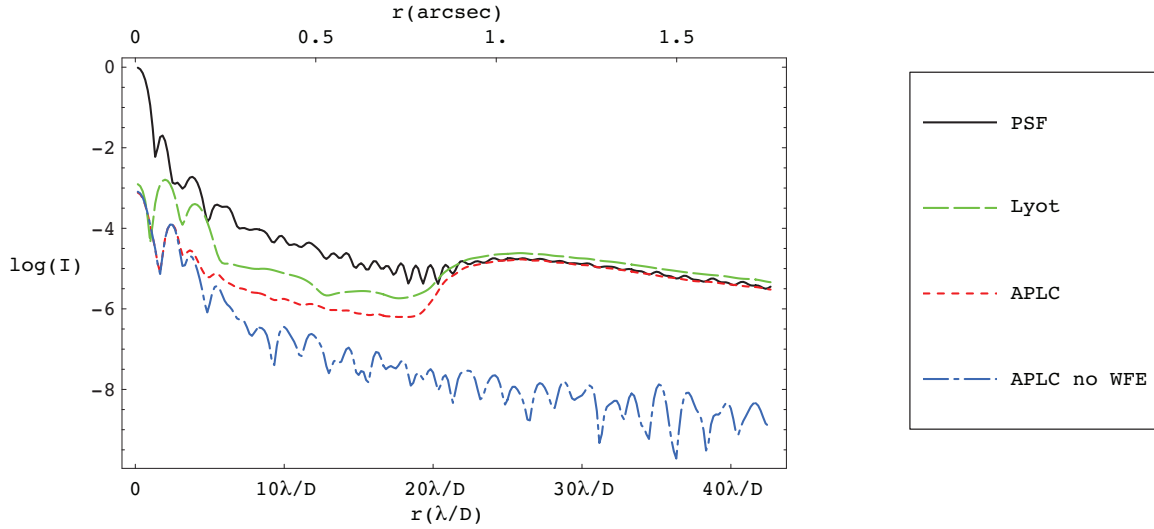0   10λ/D   20λ/D   30λ/D   40λ/D

r(λ/D)

Figure 6: Logarithm of the radially averaged intensity of the GPI *H*-band PSF, 0.5-second exposure. The PSFs are normalized so that an unocculted/off-axis PSF has a peak intensity of 1 (log(I)=0). The first three curves represent closed-loop GPI performance in which output wavefronts from a full AO simulation are fed into a coronagraph model. The top curve is the PSF without coronagraphic suppression. The next two curves compare the performance of a APLC and a classic LC, both with mask diameter of of 4.5 λ/*D* and throughput 50-60%. The blue curve represents the APLC in the absence of wave front errors for the *H* band. The FWHM of the APLC PSF compared to the clear aperture is increased by 10% with a 4.5 λ/*D* mask.

Focal Plane
Mask Wheel

Calibration
Reference Arm

Alignment /
Calibration
Beamsplitter

Alignment
Camera

Spatial Filter

Science /
Calibration
Beamsplitter   Shutter   Shutter
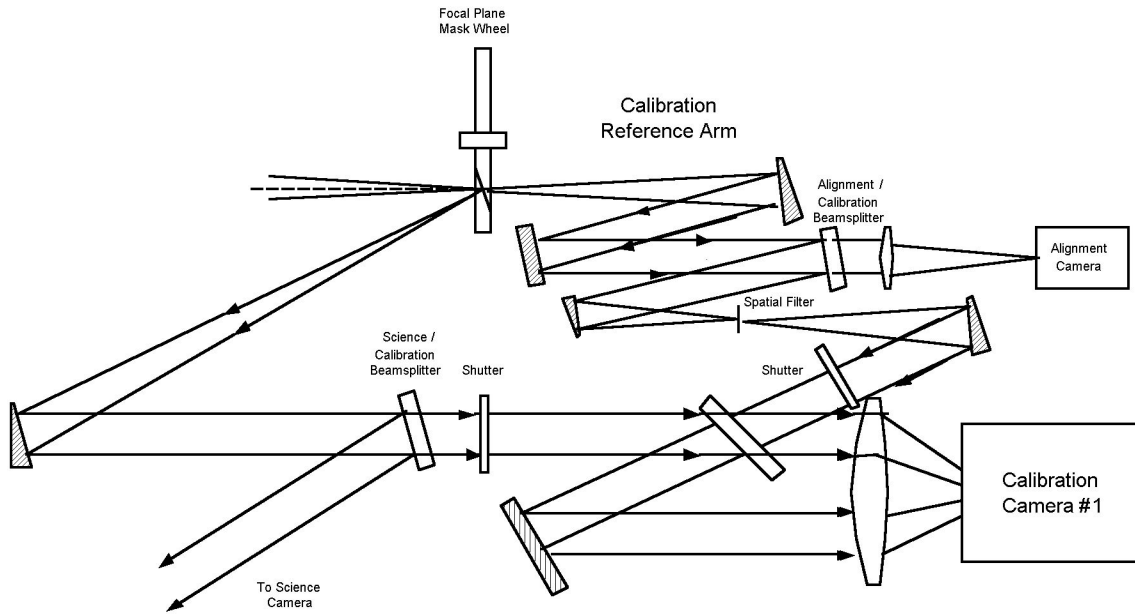
Calibration
Camera #1

To Science
Camera

Figure 7: A simple illustration of the calibration system. The science beam is on the left hand side of the image, while the reference arm and alignment and calibration camera are on the right. The path lengths are matched to within a few microns. The alignment camera insures the PSF is centered on the occulting mask. The calibration camera measures the wave front of the in the science beam.

Locating the calibration system after the occulter simplifies its operation. The coronagraph FPM acts to convert phase errors into amplitude errors, so the measurement does not require high accuracy in phase and any wavefront errors after the FPM will have little effect. This sensor will measure the wavefront at the science wavelength at ~100 Hz and time-average it over 1-10 second intervals to remove atmospheric effects (Figure 8). The reconstructed wavefront is then

propagated forward to a set of offset commands for the primary AO system. Since the sensor can only see modes that come from the wings of the PSF, it is blind to tip/tilt and low-order modes. A separate pointing sensor/low-order wavefront sensor will track these modes.
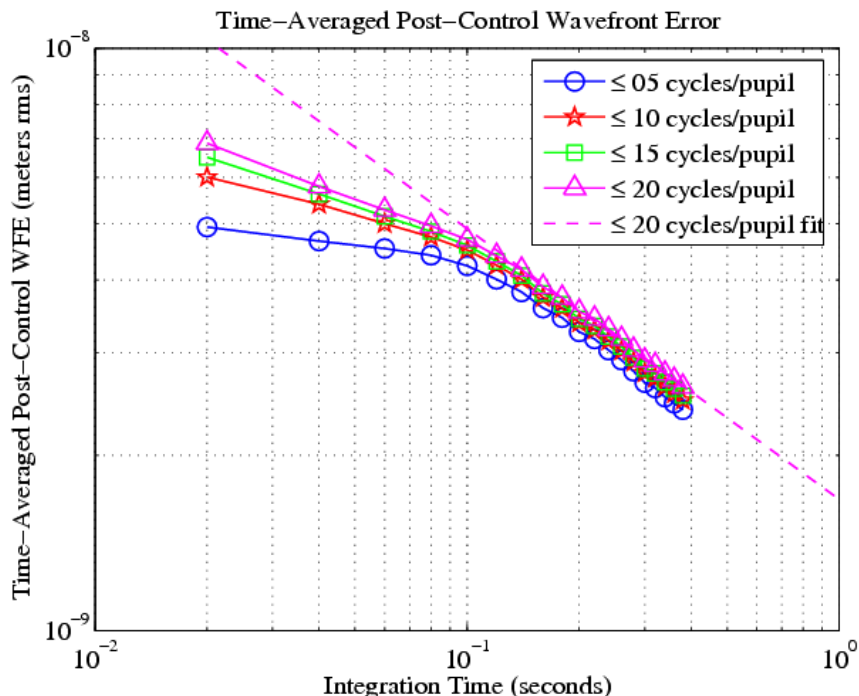

Figure 8: Level of post-coronagraph wave front errors sensed by the calibration system as function of time. Wavefront phase screens representing the AO-corrected multilayer atmosphere were input into the system and the resulting wavefronts averaged. Our ability to measure residual wave front errors with the calibration system improves roughly as root time after an initial period (dependent on spatial frequency) as atmospheric errors average out.

5. INTEGRAL FIELD SPECTROGRAPH

The primary purposes of the GPI science instrument are to detect planetary companions by distinguishing them from PSF speckle noise, to record low-resolution 1-2.5 µm spectra of these planets, and to detect and measure circumstellar dust through polarization. The basic concept of multiwavelength speckle rejection has been described in several sources[11][12]. It is extremely sensitive to differential chromatic aberrations; even a small amount of differential wavefront error can produce speckle patterns that vary strongly with wavelength[13]. To minimize this, we adopt a IFS design similar to the OSIRIS Keck instrument[14], using an array of lenslets to dissect the beam before the dispersing elements. Since it is extremely difficult to scatter light between different lenslet beams, aberrations in the dispersed beam are essentially irrelevant. The price of this architecture is paid in detector real estate – individual spectra must be well-separated on the detector. To achieve a reasonable field of view (3.5 x 3.5 arcseconds) the GPI IFS design has a spectral resolution of ~40. Models show this is sufficient to measure effective temperature and surface gravity for typical planetary targets, since planets are dominated by broad molecular features.

The IFS will also include a polarimetric mode used to characterize circumstellar dust. In this mode, a cryogenic Wollaston prism will be inserted in the reimaging optic path. This will produce two images of orthogonal polarization states, each covering half the field of view. An external half-wave plate will be used as a polarization modulator. By taking simultaneous images the (unpolarized) halo of starlight scattered by the atmosphere can be removed to see the (polarized) light reflected off circumstellar dust.

Spectrograph Camera

Detector

Reimaging Optics

Spectrograph
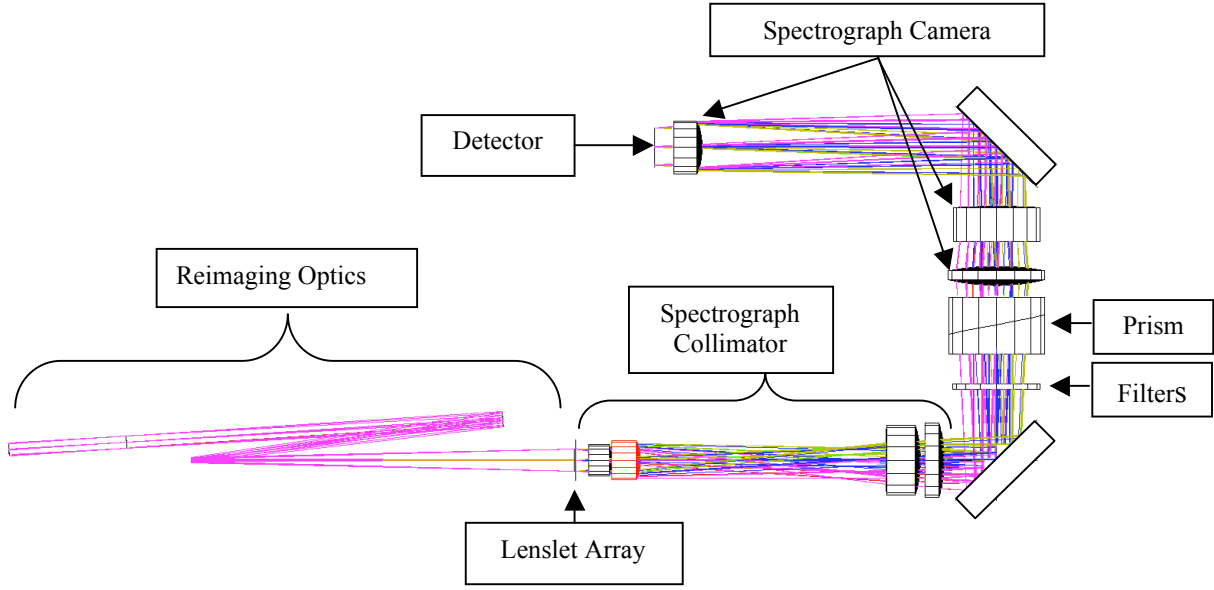Collimator

Prism

Filters

Lenslet Array

Figure 9: Raytrace of the complete IFU optical train, beginning with the entrance of the collimated coronagraph output on the left. The reimaging optics consist of two spherical mirrors used as a telephoto F/200 system. The lenslet is the smallest but most important component and dramatically speeds up the optical beam properties making the spectrograph collimator F/3.3. The spectrograph is an all refractive design with a two element prism used for dispersion. To improve the optical wavefront to the lenslet array, the filter has been placed in the spectrograph optics where it has essentially no impact on image quality. We are also exploring reflective spectrograph designs.

6. ERROR BUDGET AND SIMULATIONS

Verifying the performance of a high-contrast AO system through simulation is challenging. Many small static effects – e.g. uncalibrated non-common-path errors – only begin to significantly impact the PSF in multi-minute exposures, far too long for practical simulation. We therefore have taken a multilayered approach to simulation. Numerical simulations of the full AO system are used to evaluate performance of AO and coronagraph components in rejecting atmospheric wavefront errors and in evaluating performance as a function of star magnitude Contrast is evaluated in these simulations as the standard deviation of a given λ/D patch from its neighbors, including both Poisson noise from photon statistics and (usually dominant) residual speckles in the PSF. Residual speckles due to atmospheric sources will average out on a timescale $\sim D_{tel}/v_{wind}$;[15] speckles from AO wavefront measurement errors will average out more rapidly, while speckles from quasi-static sources such as non-common-path errors are assumed to neither average out nor be subtracted from reference PSFs. Static optical effects are evaluated with stand-along simulations and their contrast effects added independently. This approach neglects correlations between different error sources but in the regime of small wavefront errors, where the second-order "halo" term of the PSF dominates[7], these are minimal. Through this approach, it is clear that much of the improvement in "extreme" AO systems will come not from high basic Strehl ratio but from identifying and minimizing sources of quasi-static wavefront errors. Figure 10 shows the predicted performance for both dynamic (atmosphere/AO) and one class of static effects.

To evaluate the magnitude of different effects – including amplitude errors such as internal or external scintillation – we use a purely analytic error budget. Figure 11 shows a realization of one such error budget. Dominant error sources are WFS measurement noise and internal static errors. In particular, internal phase-induced intensity errors from optics at non-pupil conjugates are potentially the largest source of quasi-static speckles – "internal scintillation". These were evaluated through numerical wave-optics propagation (cross-checked with analytic calculations – see Figure 12.) To reduce these to an acceptable level, each GPI optic will be manufactured to ~5 nm RMS wavefront error. Such quality is an order of magnitude worse than the best current aspheric optics developed for applications such as extreme UV

lithography, and within the reach of commercial manufacturers for the 2-5 cm optics in GPI. The Gemini tertiary mirror induces similar errors, but since it is relatively far from focus, its effects are less severe even though its quality is lower. These effects are particularly troublesome in that they may produce speckle patterns whose radial scaling is more complex than pupil-plane errors and hence be more difficult to subtract with multiwavelength techniques[16].
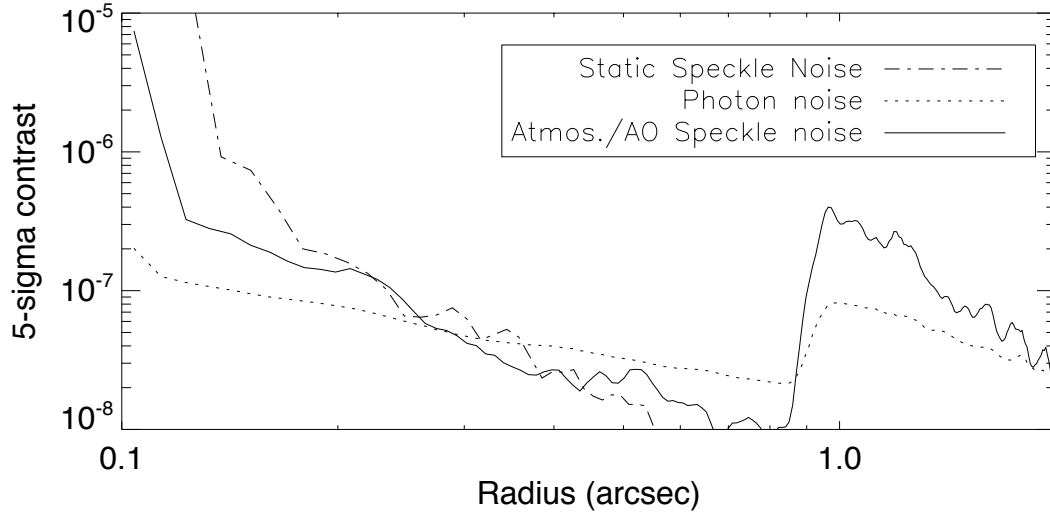

Figure 10: Contrast vs radius from GPI simulations of a 1-hour *H* integration on a *I*=6 mag. target star in a Cerro Pachaon r_0=15 cm atmosphere with 1 nm of additional static wavefront error. Curves show the residual noise due to photon statistics, atmosphere/AO speckles, and quasi-static speckles. No post-processing or speckle suppression is assumed.
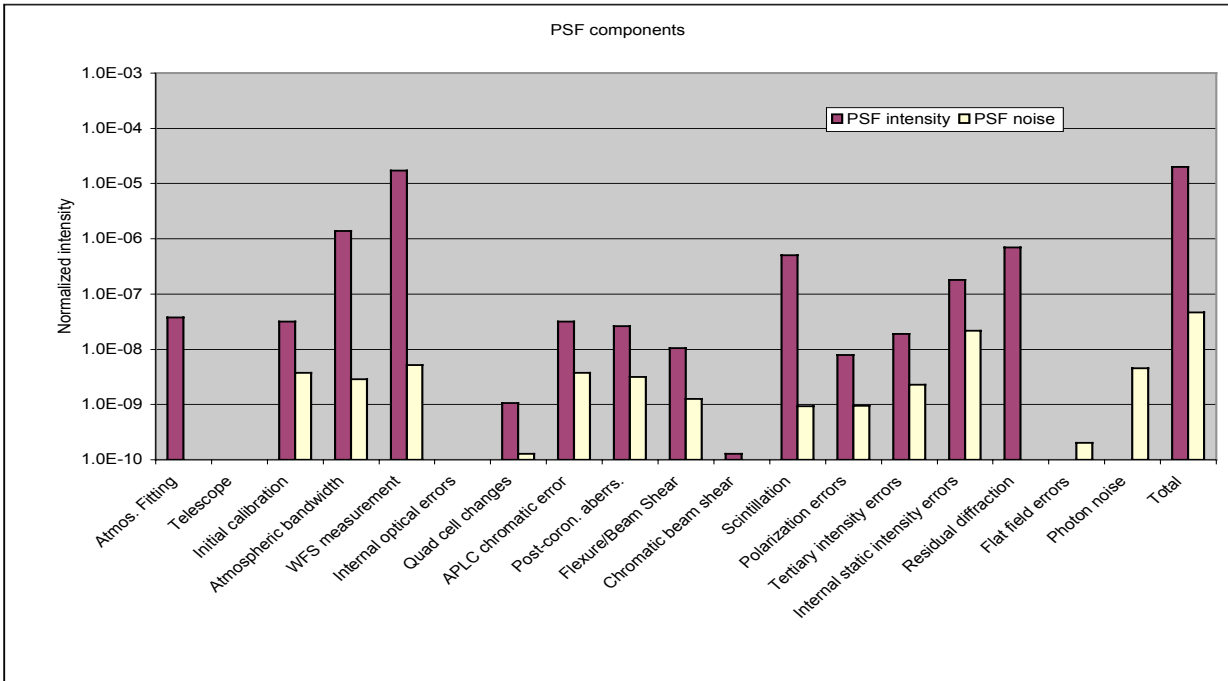

Figure 11: Analytic error budget evaluating contrast for a typical science target. For each error source, the bar graph shows the average intensity of the scattered light and the magnitude of the final noise it contributes to the PSF in a 3600-second *H*-band exposure.

Effect of Tinsley PSD on lens on halo intensity
$f^{-2.5}$ power-law psd
4.5 nm rms between 4 and 24 cycles over diameter
λ_{SC}=1.65 µm λ_{WS}=1.65 µm
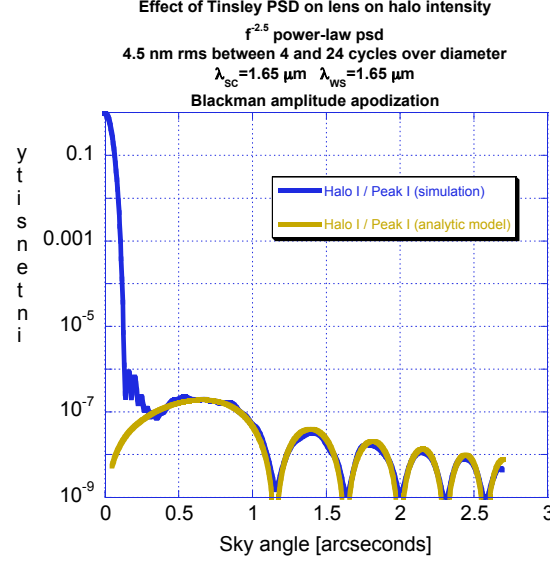**Blackman amplitude apodization**

Figure 12: Numerical simulation and analytic model of contrast degradation from phase-induced intensity errors on the first collimating optic. This simulation assumes 4.5 nm RMS wavefront error at mid spatial frequencies. Final contrast was evaluated using a simple Blackman-apodized coronagraph.

7.   CONCLUSIONS

We are currently planning for first light in late 2010. When deployed, the Gemini Planet Imager – together with its European counterpart[17] - should be capable of achieving contrast 1-2 orders of magnitude better than current AO systems. This performance improvement – comparable to the gain from CCDs over photographic plates – is achieved not just through maximizing Strehl ratio but through careful minimization and control of static and quasi-static wavefront errors. GPI will be capable of observing a large sample of targets to I=8 magnitude and imaging young or massive planets around targets in young associations and the solar neighborhood. Combining the numerical simulations discussed above with Monte Carlo models of the planet and star populations, we can predict the planet discovery rate for various assumptions. Figure 13 shows a representative outcome from one such simulation, in which the existing Doppler planet distribution is extrapolated from 5-50 AU at a rate of one giant planet per target star. A survey of 500 stars in the solar neighborhood selected to have age below 2 Gyr would discover ~100 planets.
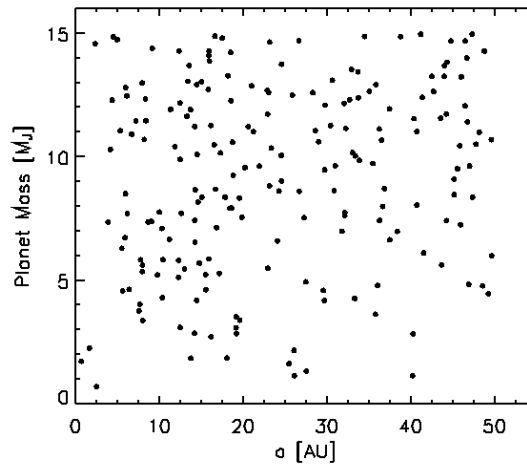

Figure 13: The distribution of GPI-detected exoplanets in the semimajor axis/exoplanet mass plane. The detected planets are drawn from the field survey of nearby (< 50 pc) stars (no age cut). This experiment samples semimajor axes and masses with uniformity.

ACKNOWLEDGEMENTS

REFERENCES

1.   See for example http://exoplanets.org/

2.   G. Chauvin et al., "A giant planet candidate near a young brown dwarf. Direct VLT/NACO observations using IR wavefront sensing", *A&A* 425, L29 (2004)

3.   Poyneer, L., and Macintosh, B., "Spatially-filtered wave-front sensor for high-order adaptive optics", *JOSA A*, 21, 810 (2004)

4.   Hartmann, R., et al., "Results of a fast pnCCD detector system", Proc. SPIE 5903, 210 (2005)

5.   Poyneer, L., and Veran, J.-P., "Optimal modal Fourier transform wavefront control", JOSA A 22, 1515 (2005)

6.   Evans, J., et al., "Extreme adaptive optics testbed: performance and characterization of a 1024-actuator MEMS deformable mirror", Proc. SPIE 6113, 131 (2006)

7.   Perrin, M., et al., "The structure of High Strehl Ratio Point-Spread Functions", Ap.J. 596, 702 (2003)

8.   Kuchner, M., and Traub, W., "A coronagraph with a band-limited mask for finding terrestrial planets", Ap.J. 570, 900 (2002)

9.   Soummer, R., "Apodized Pupil Lyot Coronagraphs for Arbitrary Telescope Apertures", Ap.J. 618, L161 (2005)

10.   Wallace, J.K., et al., "Science camera calibration for extreme adaptive optics", Proc. SPIE 5490, 370 (2004)

11.   Marois, C., et al., "Efficient Speckle Noise Attenuation in Faint Companion Imaging", PASP 117, 91 (2000)

12.   Sparks, W., and Ford, H., "Imaging spectroscopy for Extrasolar Planet Detection", Ap.J. 578, 543 (2002)

13.   Marois, C., et al., "TRIDENT: An Infrared Differential Imaging Camera Optimized for the Detection of Methanated Substellar Companions", PASP 117, 745 (2005)

14.   Larkin, J., et al., "OSIRIS: Integral field spectrograph for the Keck adaptive optics system", Proc. SPIE 4841, 1600 (2003)

15.   Macintosh, B., et al., "Speckle lifetimes in high-contrast adaptive optics", Proc. SPIE 5903, 170 (2005)

16.   Marois, C., Phillion, D., and Macintosh, B., "Exoplanet detection with simultaneous spectral differential imaging: effects of out-of-pupil-plane optical aberrations", Proc. SPIE 6269 in press (2006)

17.   Fusco, T., et al., "Design of the extreme AO system for the Planet Finder instrument on the VLT", Proc. SPIE 6272 in press (2006)